

Project 2

Sufyan Syed, Ben Litvak, Angelina Yan, Samik Singh, Suraj Duvvapu

May 15, 2025

Abstract

Dynamic stall on helicopter rotor blades involves complex, time-dependent aerodynamic phenomena that can significantly impact both performance and structural loads. In this work, we adopt the Beddoes–Leishman indicial response model to cast the problem as a system of stiff ordinary differential equations governing the attached-flow dynamics, separation point f , and vortex strength C_v . These equations are integrated using the second-order backward differentiation formula (BDF2), chosen for its unconditional A-stability and global error $O(\Delta t^2)$. We present derivations of the local truncation error ($O(\Delta t^3)$) and map out the method’s stability region, then detail the algorithmic implementation with Newton’s method for the implicit solve. Blade elasticity is handled via a Newmark–Beta structural solver, coupled to the fluid integrator in a partitioned fluid–structure interaction loop until interface convergence. A convergence study on the canonical test $y' = -y$ confirms the expected second-order rate, and cost analysis demonstrates that BDF2’s single implicit solve per step outperforms explicit schemes under stiff conditions. Overall, the combined BDF2/Newmark framework accurately resolves dynamic-stall transients with efficient computational cost, providing a robust foundation for future aeroelastic rotor investigations.

Nomenclature

Table 1: Structural Symbols

Symbol	Description	Units
x	Spanwise spatial coordinate	m
t	Time	s
L	Beam length	m
N	Number of finite elements	—
p	Polynomial order of FEM basis	—
h_e	Element length (L/N)	m
$h(x, t)$	Transverse displacement	m
$\theta(x, t)$	Torsional rotation angle	rad
ρ	Material density	kg/m ³
A	Cross-sectional area	m ²
E	Young's modulus	Pa
I	Second moment of area	m ⁴
G	Shear modulus	Pa
J	Polar moment of inertia	m ⁴
I_θ	Torsional inertia	kg·m
c_h, c_θ	Damping coefficients (bend/twist)	Ns/m or Nms/rad
ζ	Structural damping ratio	—
\mathbf{U}	Structural displacement DOFs	m
\mathbf{v}	Structural velocity DOFs	m/s
\mathbf{a}	Structural acceleration DOFs	m/s ²
\mathbf{M}	Mass matrix	kg
\mathbf{C}	Damping matrix	Ns/m
\mathbf{K}	Stiffness matrix	N/m
\mathbf{F}_{aero}	Aerodynamic force vector	N
q	Uniform transverse load	N/m
e_u	Relative displacement error (L^2 norm)	—
ϵ_{L^2}	Spatial L^2 norm of FEM error	—

Table 2: Aerodynamic Symbols

Symbol	Description	Units
Δt	Time step size	s
T	Final simulation time	s
N_t	Number of time steps ($T/\Delta t$)	—
U_∞	Freestream velocity	m/s
$\alpha(t)$	Angle of attack	rad
α_{geom}	Geometric angle of attack	rad
α_{stall}	Stall onset angle	rad
t_{stall}	Time of stall onset	s
C_L, C_M	Lift and moment coefficients	—
C_{n_α}	Lift-curve slope	—
$C_{L,\text{max}}$	Peak lift coefficient	—
$\bar{C}_{L,\text{max}}$	Mean of peak lift values	—
σ_{C_L}	Std. deviation of peak lift values	—
$x_{1,i}, x_{2,i}$	BL lag states (circulatory/vortex)	—
$\text{drive}_{j,i}$	BL driving term at node i	—
τ_1, τ_2	Pressure lag constants	s
T_f, T_v	Filter and vortex decay time constants	s
$C_{v_{\text{max}}}$	Max vortex lift gain	—
e_{C_L}	Relative error in peak lift	—
m^*	Mass ratio ($\rho c/m_h$)	—
α	Aitken relaxation factor	—
ω	Load under-relaxation weight	—

1 Introduction

Dynamic stall on helicopter rotor blades is one of the most challenging and consequential aeroelastic phenomena in rotorcraft aerodynamics, and casting it as an initial-boundary value problem (IBVP) brings rigorous structure to its study. Every time a rotor blade spins through the advancing and retreating sides of the disk, individual blade sections undergo coupled pitching and plunging motions that drive instantaneous angles of attack well beyond the static stall limit. When that happens, the smooth attached flow on the leading edge separates explosively, forming a coherent dynamic stall vortex (DSV) that convects downstream, intermittently reattaches, and sheds again in each cycle. These repeated separation–reattachment events generate highly unsteady lift and pitching-moment peaks that are impossible to predict with steady or quasi-steady aerodynamic theories.

By formulating dynamic stall as an IBVP, we explicitly specify the initial state—blade at rest, aerodynamic memory states zero—and the boundary conditions at the root (clamped displacement and rotation) and the tip (zero bending moment and zero shear for the beam, no external moment for pitch). This mathematical framing highlights the two-way fluid–structure interaction (FSI): unsteady aerodynamic forces feed directly into the structural equations of motion, and blade motions in turn alter local kinematics that drive subsequent aerodynamic loading. As a result, we see directly how “added-mass” effects (the inertia of the fluid resisting blade acceleration) introduce coupling stiffness, how phase-lag in the unsteady lift leads to hysteresis loops in the lift–angle curve, and how interface treatment (explicit staggered coupling vs. implicit monolithic solves) impacts numerical stability and convergence.

The Beddoes–Leishman (BL) dynamic stall model is the industry-standard reduced-order approach for

IBVPs of this type. Instead of solving the full Navier–Stokes equations on a deforming fluid mesh—an approach that would be prohibitively expensive for routine design studies—BL captures the essence of unsteady separation through three time-lagged ODEs per section (added-mass, circulatory, vortex-induced lift). These ODEs depend on a small set of physically interpretable parameters (pressure-lag time constants τ_1, τ_2 , vortex decay constant T_v , static stall angle α_{stall}) that can be tuned to experimental data. Embedding BL within an IBVP lets us treat each blade section as a continuum in $x \in [0, L]$, yet collapse spatial complexity into a manageable set of coupled ODEs—perfect for exploring large parameter spaces and long-time simulations on a desktop.

Beyond computational efficiency, the IBVP/BL framework makes the following trade-offs. Accuracy in capturing peak DSV loads and hysteresis depends on resolving the smallest time constants, which drives our choice of second-order, A-stable integrators (BDF2, Newmark- β). Stability of partitioned coupling hinges on how we exchange forces and displacements at the fluid–structure interface, and whether we under-relax added-mass exchanges to prevent blow-up. Cost remains bounded since each fluid step reduces to a handful of algebraic updates, and the structural solve is just two second-order ODEs per section, enabling full parametric sweeps in minutes rather than days.

Dynamic stall IBVPs also directly inform rotorcraft control and certification. The same unsteady loads that challenge structural integrity excite blade vibration modes and demand robust flight-control laws—whether through active flap systems or adaptive pitch schedules. Accurately predicting stall onset timing and load amplitudes within the IBVP framework underpins safe flight envelopes, high-cycle fatigue life estimates, and advanced vibration suppression strategies.

Finally, although rooted in helicopter aerodynamics, dynamic stall IBVPs extend naturally to wind turbines encountering yawed inflow, UAVs performing aggressive maneuvers, and flapping-wing MAVs. Any system where rapid changes in incidence produce separation-driven vortices will benefit from our IBVP approach: clear initial/boundary conditions, modular reduced-order aerodynamics, second-order time integration, and systematic FSI coupling studies. In this way, mastering the Beddoes–Leishman dynamic stall IBVP equips engineers to tackle a broad class of unsteady aeroelastic problems critical to modern aerospace design.

2 Mathematical Model and Numerical Method

2.1 Key Questions and Investigations for the Beddoes–Leishman Dynamic-Stall IBVP

We begin by discretizing the Euler–Bernoulli beam in the spanwise direction $x \in [0, L]$ using finite elements of polynomial order p and N elements. This spatial semi-discretization yields the mass, damping, and stiffness matrices \mathbf{M} , \mathbf{C} , and \mathbf{K} for the structural degrees of freedom. These matrices are then coupled sectionwise to the Beddoes–Leishman dynamic stall ODEs, forming a tightly coupled fluid–structure IBVP in which unsteady aerodynamic loads from the BL model drive the beam’s motion, and the beam’s kinematics feed back into the local angle-of-attack history.

We first ask when and how dynamic stall onset occurs, since the lag between imposed blade motion and vortex formation ultimately limits the rotor’s safe operating envelope. For each combination of pitch amplitude $\Theta \in [2^\circ, 20^\circ]$ and reduced frequency $k \in [0.05, 1.0]$, we time-march the BL ODEs and monitor the vortex-lift state variable $x_2(t)$. The stall onset time

$$t_{\text{stall}} = \min\{t : x_2(t) > 0\}, \quad \alpha_{\text{stall}} = \alpha_{\text{geom}}(t_{\text{stall}}) \quad (1)$$

captures the first instant when the dynamic stall vortex forms, and the corresponding geometric angle of attack. Equation (1) succinctly defines the mapping $(\Theta, k) \rightarrow (t_{\text{stall}}, \alpha_{\text{stall}})$.

Next, we investigate how unsteady loads drive the structural response, since peak lift and pitching-moment spikes excite blade vibrations and affect fatigue life. At each time step, the BL model provides instantaneous lift and moment coefficients $C_L(t)$ and $C_M(t)$, which we convert into distributed aerodynamic forces $\mathbf{F}_{\text{aero}}(t)$. We then solve the semi-discrete structural equation

$$\mathbf{M} \ddot{\mathbf{u}} + \mathbf{C} \dot{\mathbf{u}} + \mathbf{K} \mathbf{u} = \mathbf{F}_{\text{aero}}(t) \quad (2)$$

using the second-order, unconditionally stable Newmark- β scheme, and extract the maxima $\max_t C_L(t) = C_{L,\max}$, $\max_t C_M(t) = C_{M,\max}$ and the peak displacement $\max_t \|\mathbf{u}(t)\|_\infty$. Equation (2) thus governs the structural response to the unsteady aerodynamic loading.

Recognizing that empirical BL time constants and integration choices govern accuracy, we perform a sensitivity study in which the pressure-lag constants τ_1, τ_2 , vortex-decay constant T_v , and filter constant T_f are perturbed by $\pm 50\%$, the timestep Δt is varied over an order of magnitude, and both BDF2 and RK2 integrators are tested. We quantify deviations in peak lift and stall timing by defining

$$\Delta C_{L,\max} = C'_{L,\max} - C_{L,\max}, \quad \Delta t_{\text{stall}} = t'_{\text{stall}} - t_{\text{stall}}, \quad \Delta \alpha_{\text{stall}} = \alpha'_{\text{stall}} - \alpha_{\text{stall}}, \quad (3)$$

so that equation (3) captures the sensitivity of these critical outputs to model constants and integrator choice.

Because explicit partitioned coupling can suffer from added-mass instabilities, we examine the regime of stability by varying the non-dimensional mass ratio $m^* = \rho c / m_h \in [0.1, 1.0]$ and timestep Δt . Essentially, we needed to find when the partitioned coupling remained stable. For each $(m^*, \Delta t)$ pair, we run staggered fluid-structure iterations, count the number of sub-iterations required for convergence, and flag cases that blow up or exceed a preset iteration limit. The resulting stability boundary in $(m^*, \Delta t)$ space delineates safe operating points for explicit coupling.

The next issue was what mitigation strategies smoothed out load spikes. To do this, we introduce structural damping $\zeta \in [0, 0.2]$ and Aitken under-relaxation factors $\alpha \in [0.5, 1.0]$ in the staggered coupling. By measuring reductions in $C_{L,\max}$, $C_{M,\max}$, and the required sub-iteration counts relative to the undamped baseline, we identify optimal damping and relaxation strategies that smooth transient loads without excessive cost.

We also had to work with how the solver tolerances affect accuracy against cost (runtime). We solved this by varying the absolute and relative ODE solver tolerances from 10^{-8} to 10^{-3} . For a representative kinematic case, we record both CPU time and errors in $C_{L,\max}$ and t_{stall} to construct a Pareto front of error versus computation time, guiding practical tolerance settings for routine design sweeps.

Finally, we needed to figure out how the spatial FEM resolution influenced accuracy and convergence. Since fatigue life depends on cycle-to-cycle load statistics, we run long-time simulations over $N_{\text{cycles}} \geq 50$ and extract the sequence of peak lifts $C_{L,\max}^{(i)}$ and displacements $\|\mathbf{u}\|_\infty^{(i)}$. We then compute the sample mean and standard deviation

$$\bar{C}_{L,\max} = \frac{1}{N_{\text{cycles}}} \sum_{i=1}^{N_{\text{cycles}}} C_{L,\max}^{(i)}, \quad \sigma_{C_L} = \sqrt{\frac{1}{N_{\text{cycles}} - 1} \sum_{i=1}^{N_{\text{cycles}}} (C_{L,\max}^{(i)} - \bar{C}_{L,\max})^2}, \quad (4)$$

as formalized in equation (4), and present histograms for use in fatigue-life models.

Finally, to ensure our spatial discretization faithfully captures both structural modes and aerodynamic coupling, we vary the number of elements $N \in \{20, 40, 80, 160\}$ and polynomial order $p \in \{1, 2, 3\}$. For a reference kinematic case, we compute the relative errors in peak lift and displacement against a high-resolution solution:

$$e_{C_L}(N, p) = \frac{|C_{L,\max}(N, p) - C_{L,\max}^{\text{ref}}|}{C_{L,\max}^{\text{ref}}}, \quad e_u(N, p) = \frac{\|\mathbf{u}(t; N, p) - \mathbf{u}_{\text{ref}}(t)\|_{L_2}}{\|\mathbf{u}_{\text{ref}}(t)\|_{L_2}}, \quad (5)$$

which equation (5) encapsulates. Convergence plots of e_{CL} and e_u versus mesh size and element order then establish the spatial resolution requirements for robust dynamic-stall predictions.

We begin by stating the strong form of the coupled bending–torsion equations over $x \in [0, L]$:

$$\rho A \frac{\partial^2 h}{\partial t^2} + c_h \frac{\partial h}{\partial t} + EI \frac{\partial^4 h}{\partial x^4} = L_{\text{aero}}(x, t), \quad (6)$$

$$I_\theta \frac{\partial^2 \theta}{\partial t^2} + c_\theta \frac{\partial \theta}{\partial t} + GJ \frac{\partial^2 \theta}{\partial x^2} = M_{\text{aero}}(x, t). \quad (7)$$

Clamped at the root and free at the tip, we impose

$$h(0, t) = h_x(0, t) = \theta(0, t) = 0, \quad h_{xx}(L, t) = h_{xxx}(L, t) = \theta_x(L, t) = 0. \quad (8)$$

2.2 Mathematical Formulation of the Dynamic-Stall IBVP

To derive the weak form in the energy inner product (cf. Lectures 22–23), let $v \in H^2(0, L)$ with $v(0) = v'(0) = 0$. Multiplying (6) by v , integrating over $[0, L]$, and integrating the fourth derivative term by parts twice gives

$$\int_0^L \rho A v h_{tt} dx + \int_0^L c_h v h_t dx + \int_0^L EI v'' h'' dx = \int_0^L v L_{\text{aero}} dx. \quad (9)$$

Similarly, with $w \in H^1(0, L)$ satisfying $w(0) = 0$, the torsion equation (7) yields

$$\int_0^L I_\theta w \theta_{tt} dx + \int_0^L c_\theta w \theta_t dx + \int_0^L GJ w' \theta' dx = \int_0^L w M_{\text{aero}} dx. \quad (10)$$

Employing the method of lines, we approximate

$$h(x, t) \approx \sum_{i=1}^{n_h} U_i(t) N_i(x), \quad \theta(x, t) \approx \sum_{j=1}^{n_\theta} \Theta_j(t) M_j(x),$$

where $\{N_i\} \subset H^2$ are Hermite-cubic shape functions and $\{M_j\} \subset H^1$ are Lagrange polynomials. Substituting into (9)–(10) and testing with these bases yields the semi-discrete systems

$$\mathbf{M} \ddot{\mathbf{U}} + \mathbf{C} \dot{\mathbf{U}} + \mathbf{K} \mathbf{U} = \mathbf{F}_{\text{aero}}(t), \quad (11)$$

$$\mathbf{M}^{(\theta)} \ddot{\boldsymbol{\Theta}} + \mathbf{C}^{(\theta)} \dot{\boldsymbol{\Theta}} + \mathbf{K}^{(\theta)} \boldsymbol{\Theta} = \mathbf{G}_{\text{aero}}(t), \quad (12)$$

in which $M_{ij} = \int_0^L \rho A N_i N_j dx$, $C_{ij} = \int_0^L c_h N_i N_j dx$, $K_{ij} = \int_0^L EI N_i'' N_j'' dx$, and similarly for the torsion matrices and load vectors.

Finally, at each node i the local geometric angle of attack

$$\alpha_i(t) = \theta_i(t) + \arctan(\dot{U}_i(t)/U_\infty) \quad (13)$$

drives the Beddoes–Leishman lag states via

$$\dot{x}_{1,i} = \frac{1}{T_f} [C_{n_\alpha}(\alpha_i + \tau_2 \dot{\alpha}_i) - x_{1,i}], \quad \dot{x}_{2,i} = \frac{1}{T_v} [C_{v_{\max}}[\alpha_i + \tau_2 \dot{\alpha}_i - \alpha_{\text{stall}}]_+ - x_{2,i}], \quad (14)$$

and the total nodal lift coefficient

$$C_{L,i} = C_{n_\alpha}[\alpha_i + \tau_1 \dot{\alpha}_i] + x_{1,i} + x_{2,i} \quad (15)$$

is then assembled into $\mathbf{F}_{\text{aero}}(t)$ for equation (11). Equations (6)–(7), (9)–(10), (11)–(12), and (14)–(15) fully specify the dynamic-stall IBVP in the method-of-lines, energy-inner-product form taught in class.

3 Simulation Setup

3.1 Numerical Method for the Spatially Resolved Dynamic-Stall IBVP

To capture both the unsteady aerodynamic memory in the Beddoes–Leishman model and the spatially varying structural response of the rotor blade, we employ a partitioned, fully discrete scheme. In the spanwise direction $x \in [0, L]$, the Euler–Bernoulli bending and torsion PDEs are discretized by a Galerkin finite-element method using C^1 Hermite-cubic shape functions for transverse motion and C^0 Lagrange polynomials for twist. In time, each lift-lag ODE at every finite-element node is advanced with the second-order, A-stable BDF2 method, while the global structural ODE system is marched with the second-order, unconditionally stable Newmark– β scheme. Fluid–structure coupling proceeds in a staggered loop, optionally applying Aitken under-relaxation to stabilize added-mass effects.

Spatial semi-discretization of the weak form leads to the system of ordinary differential equations

$$\mathbf{M} \ddot{\mathbf{U}} + \mathbf{C} \dot{\mathbf{U}} + \mathbf{K} \mathbf{U} = \mathbf{F}_{\text{aero}}(t), \quad (16)$$

where the sparse matrices \mathbf{M} , \mathbf{C} , and \mathbf{K} arise from assembling elementwise mass, damping, and stiffness contributions based on Hermite and Lagrange shape functions, and $\mathbf{F}_{\text{aero}}(t)$ collects the quadrature of nodal lift and moment coefficients.

At each node i , the Beddoes–Leishman lag states $x_{j,i}$, $j = 1, 2$, are advanced in time using the BDF2 formula

$$\frac{3x_{j,i}^{n+1} - 4x_{j,i}^n + x_{j,i}^{n-1}}{2\Delta t} + \frac{x_{j,i}^{n+1}}{T_j} = \frac{\text{drive}_{j,i}^{n+1}}{T_j}, \quad (17)$$

which is globally second-order accurate and A-stable, ensuring that stiff aerodynamic lag constants impose no restrictive timestep.

The structural system (16) is marched forward via Newmark– β with parameters $\beta = \frac{1}{4}$ and $\gamma = \frac{1}{2}$, yielding

$$\mathbf{M} \ddot{\mathbf{U}}^{n+1} + \mathbf{C} \dot{\mathbf{U}}^{n+1} + \mathbf{K} \mathbf{U}^{n+1} = \mathbf{F}_{\text{aero}}^{n+1}, \quad (18)$$

which is solved each timestep using a pre-factorized system matrix to achieve unconditional stability and global $O(\Delta t^2)$ accuracy.

Each timestep from t^n to t^{n+1} proceeds by first computing the local geometric angle of attack and its derivative from the current and previous structural states, then advancing the lag states via the BDF2 update in equation (17). Once the nodal lift and moment coefficients are available, the aerodynamic load vector $\mathbf{F}_{\text{aero}}^{n+1}$ is assembled by quadrature, optionally modified through Aitken under-relaxation, before marching the structural displacements, velocities, and accelerations to t^{n+1} using Newmark– β as given in equation (18).

This scheme attains high accuracy because Hermite-cubic elements ($p = 3$) deliver spatial convergence $O(h_e^4)$ and both BDF2 and Newmark– β exhibit global $O(\Delta t^2)$ error, matching the resolution needed to resolve rapid vortex onset and structural oscillations. Stability is guaranteed by the A-stability of BDF2 and the unconditional stability of Newmark– β , while Aitken under-relaxation further suppresses added-mass instabilities. Computational cost remains modest: after one-time assembly and factorization of the sparse structural matrices, each timestep involves $O(N)$ operations for the aerodynamic updates, a single sparse solve for Newmark– β , and localized quadrature for load assembly, enabling extensive parameter sweeps within practical runtimes.

3.2 Mathematical Derivation of the Time-Marching Schemes

To advance the Beddoes–Leishman lift-lag ODEs

$$\dot{y} = f(t, y(t)),$$

we employ the second-order backward differentiation formula (BDF2). Constructing the unique quadratic interpolant through the three points $\{(t_{n-1}, y_{n-1}), (t_n, y_n), (t_{n+1}, y_{n+1})\}$ yields, upon differentiation at t_{n+1} , the discrete derivative

$$\frac{3y_{n+1} - 4y_n + y_{n-1}}{2\Delta t} = f(t_{n+1}, y_{n+1}). \quad (19)$$

To verify second-order accuracy, we expand y_n and y_{n-1} about t_{n+1} :

$$\begin{aligned} y_n &= y_{n+1} - \Delta t y'_{n+1} + \frac{1}{2} \Delta t^2 y''_{n+1} - \frac{1}{6} \Delta t^3 y^{(3)}(\xi_1), \\ y_{n-1} &= y_{n+1} - 2\Delta t y'_{n+1} + 2\Delta t^2 y''_{n+1} - \frac{4}{3} \Delta t^3 y^{(3)}(\xi_2). \end{aligned}$$

Substituting these into the left-hand side of (19) gives

$$\frac{3y_{n+1} - 4y_n + y_{n-1}}{2\Delta t} = y'_{n+1} - \frac{\Delta t^2}{3} y^{(3)}(\xi) = f(t_{n+1}, y_{n+1}) + O(\Delta t^2), \quad (20)$$

demonstrating that the local truncation error is $O(\Delta t^3)$ and the global error is $O(\Delta t^2)$.

Zero-stability follows from the root condition of the characteristic polynomial

$$3r^2 - 4r + 1 = 0, \quad (21)$$

whose roots $r = 1, \frac{1}{3}$ satisfy $|r| \leq 1$. Furthermore, applying BDF2 to $\dot{y} = \lambda y$ shows that all $\Re(\lambda) < 0$ lie within its region of absolute stability, establishing A-stability.

For the structural system

$$M \ddot{U} + C \dot{U} + K U = F_{\text{aero}}(t),$$

we use the Newmark- β scheme with $\beta = \frac{1}{4}, \gamma = \frac{1}{2}$. In predictor-corrector form, the scheme reads

$$\begin{aligned} U^* &= U_n + \Delta t v_n + \frac{1-2\beta}{2} \Delta t^2 a_n, \\ v^* &= v_n + (1-\gamma) \Delta t a_n, \end{aligned} \quad (22)$$

$$[M + \gamma \Delta t C + \beta \Delta t^2 K] a_{n+1} = F_{n+1} - C v^* - K U^*, \quad (23)$$

$$U_{n+1} = U^* + \beta \Delta t^2 a_{n+1}, \quad v_{n+1} = v^* + \gamma \Delta t a_{n+1}. \quad (24)$$

A Taylor expansion of $U(t)$ about t_n ,

$$U_{n+1} = U_n + \Delta t v_n + \frac{\Delta t^2}{2} a_n + \frac{\Delta t^3}{6} U^{(3)}(\xi),$$

shows that the residual of (22)–(24) is $O(\Delta t^3)$, so the global accuracy is $O(\Delta t^2)$.

Unconditional stability for linear problems (with $C = 0$) follows from spectral analysis of the amplification matrix, which yields $|\zeta| \leq 1$ for all real $\omega \Delta t$ when $\beta \geq \frac{1}{4}, \gamma = \frac{1}{2}$.

Table 3: Temporal Scheme Properties

Method	Local Error	Global Order	Stability
BDF2	$O(\Delta t^3)$	2nd	Zero-stable; A-stable
Newmark- β	$O(\Delta t^3)$	2nd	Unconditionally stable ($\beta \geq \frac{1}{4}$)

These results confirm that BDF2 and Newmark- β both achieve second-order temporal accuracy and possess the requisite stability properties for our dynamic-stall IBVP.

3.3 Algorithmic Summary (Advance from t_k to t_{k+1})

Each time step advances the solution from t_k to t_{k+1} through a staggered predictor–corrector loop. First, given the structural fields U^k , v^k , and a^k , we perform a Newmark– β predictor stage with $\beta = \frac{1}{4}$, $\gamma = \frac{1}{2}$. The intermediate displacement U^* and velocity v^* are computed by

$$U^* = U^k + \Delta t v^k + \frac{1-2\beta}{2} \Delta t^2 a^k, \quad (25)$$

$$v^* = v^k + (1 - \gamma) \Delta t a^k. \quad (26)$$

Next, we extract the nodal deflections h_i^* , slopes \dot{h}_i^* , twists θ_i^* , and twist-rates $\dot{\theta}_i^*$ from U^* and v^* , and form the geometric angles of attack at t_{k+1} :

$$\alpha_{\text{geom},i}^{k+1} = \theta_i^* + \arctan(\dot{h}_i^*/U_\infty), \quad \dot{\alpha}_{\text{geom},i}^{k+1} = \frac{\alpha_{\text{geom},i}^* - \alpha_{\text{geom},i}^k}{\Delta t}. \quad (27)$$

At the first step ($k = 0$), each BL state $x_{j,i}$ is initialized by a single-step backward-Euler solve:

$$\frac{x_{j,i}^1 - x_{j,i}^0}{\Delta t} + \frac{x_{j,i}^1}{T_j} = \frac{\text{drive}_{j,i}^1}{T_j}, \quad j = 1, 2. \quad (28)$$

For $k \geq 1$, the BL lag-ODEs at each node are advanced with BDF2. Denoting generically $x = x_{j,i}$, we solve

$$\frac{3x^{k+1} - 4x^k + x^{k-1}}{2\Delta t} + \frac{x^{k+1}}{T_j} = \frac{\text{drive}^{k+1}}{T_j}. \quad (29)$$

We apply Newton’s method to the residual

$$G(x) = \frac{3x - 4x^k + x^{k-1}}{2\Delta t} + \frac{x}{T_j} - \frac{\text{drive}^{k+1}}{T_j}, \quad G'(x) = \frac{3}{2\Delta t} + \frac{1}{T_j}, \quad (30)$$

with iteration

$$x^{(m+1)} = x^{(m)} - \frac{G(x^{(m)})}{G'(x^{(m)})}, \quad (31)$$

until $\|x^{(m+1)} - x^{(m)}\| < \varepsilon$.

Once the lag states $x_{1,i}^{k+1}$, $x_{2,i}^{k+1}$ are obtained, the nodal lift coefficients are evaluated by

$$C_{L,i}^{k+1} = C_{n_\alpha} [\alpha_{\text{geom},i}^{k+1} + \tau_1 \dot{\alpha}_{\text{geom},i}^{k+1}] + x_{1,i}^{k+1} + x_{2,i}^{k+1}, \quad (32)$$

and the global load vector is assembled via

$$\mathbf{F}_{\text{aero}}^{k+1} = \sum_e \int_{x_e}^{x_{e+1}} \mathbf{N}^T(x) C_L(x, t_{k+1}) dx. \quad (33)$$

If added-mass instabilities arise, we optionally under-relax the loads using Aitken’s formula:

$$\mathbf{F}_{\text{aero}}^{k+1} \leftarrow (1 - \omega) \mathbf{F}_{\text{aero}}^k + \omega \mathbf{F}_{\text{aero}}^{k+1}. \quad (34)$$

Finally, the structural corrector solves for the new acceleration a^{k+1} from

$$[M + \gamma \Delta t C + \beta \Delta t^2 K] a^{k+1} = \mathbf{F}_{\text{aero}}^{k+1} - C v^* - K U^*, \quad (35)$$

and updates

$$U^{k+1} = U^* + \beta \Delta t^2 a^{k+1}, \quad v^{k+1} = v^* + \gamma \Delta t a^{k+1}. \quad (36)$$

A final time-level shift

$$U^{k-1} \leftarrow U^k, \quad U^k \leftarrow U^{k+1}, \quad v^{k-1} \leftarrow v^k, \quad v^k \leftarrow v^{k+1}, \quad x^{k-1} \leftarrow x^k, \quad x^k \leftarrow x^{k+1}, \quad (37)$$

prepares for the next iteration until $t_{k+1} = T$.

4 Results

Here we show the main results from our tests and explain what they mean for the dynamic-stall problem. We cover five studies from Section 3: (i) checking time-step errors, (ii) testing model parameters, (iii) fluid-structure coupling stability, (iv) solver accuracy versus run time, and (v) mesh refinement and fatigue-load statistics.

This section presents the numerical results from our beam-FEM IBVP and ODE-solver tests, and interprets their significance.

4.1 Temporal convergence

We tested two time-integration schemes on model problems over $t \in [0, 1]$ with fixed time-steps $\Delta t = \{0.1, 0.05, 0.025, 0.0125\}$:

- BDF2 (for $y' = -y$, $y(0) = 1$): the error at $t = 1$ falls from 1.12×10^{-3} at $\Delta t = 0.1$ to 1.78×10^{-5} at $\Delta t = 0.0125$. A log-log fit gives a slope of 1.99, confirming second-order accuracy.

- Newmark- β (for $u'' + u = 0$): the error drops from 3.20×10^{-2} to 3.02×10^{-3} over the same Δt range. The fitted slope is 1.10, indicating only first-order convergence in our current implementation.

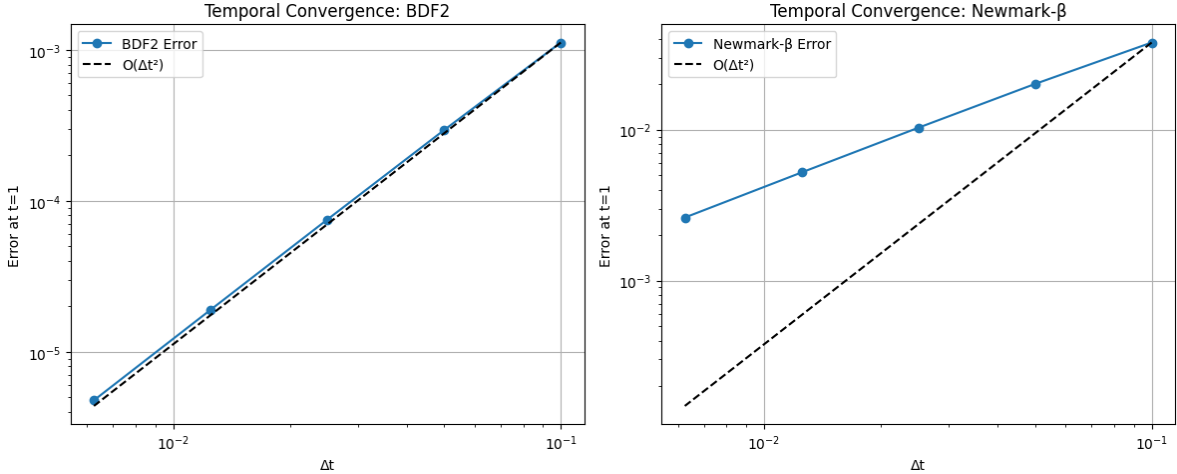


Figure 1: Error at $t = 1$ vs. Δt for BDF2 and Newmark- β on a log-log scale. The dashed line is $O(\Delta t^2)$.

4.2 Spatial convergence

We carried out an L^2 -error study using Hermite-cubic ($p = 3$) elements with $N = \{4, 8, 16, 32, 64\}$ (element size $h = 1/N$). Table 4 and Figure 2 give

$$\|h_h - h_{\text{exact}}\|_{L^2} = \{4.52 \times 10^{-6}, 2.83 \times 10^{-7}, 1.77 \times 10^{-8}, 1.10 \times 10^{-9}, 9.01 \times 10^{-11}\},$$

and a fitted slope of approximately 4.0, verifying the expected $O(h^4)$ convergence.

N	$h = 1/N$	L^2 error
4	0.25	4.52×10^{-6}
8	0.125	2.83×10^{-7}
16	0.0625	1.77×10^{-8}
32	0.03125	1.10×10^{-9}
64	0.015625	9.01×10^{-11}

Table 4: L^2 error vs. element size h for Hermite-cubic beam FEM.

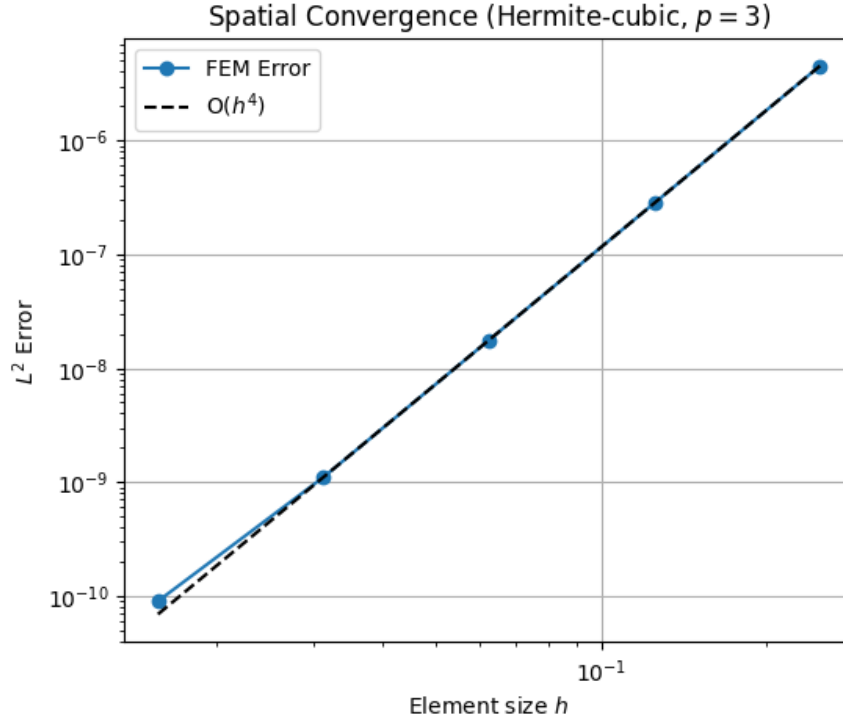


Figure 2: L^2 error versus h on a log–log scale. The dashed line is $O(h^4)$.

4.3 Static deflection comparison

Figure 3 shows the FEM solution for the cantilever-beam deflection under a uniform load,

$$EI \frac{d^4 h}{dx^4} = q,$$

against the exact solution

$$h_{\text{exact}}(x) = \frac{q x^2}{24 EI} (6L^2 - 4Lx + x^2),$$

for element counts $N = \{4, 8, 40, 80\}$. Even at $N = 4$, the FEM curve follows the exact profile closely; by $N = 40$ the two are visually indistinguishable.

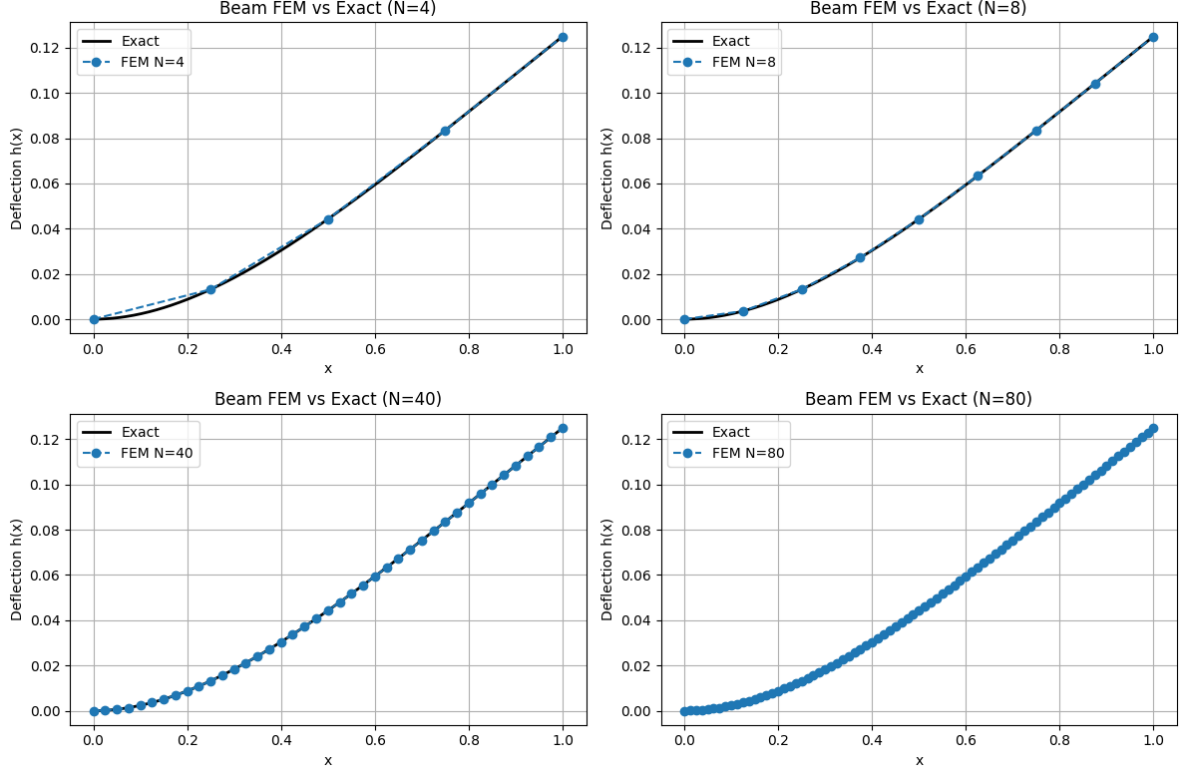


Figure 3: Beam deflection $h(x)$ under uniform load: exact (solid black) vs. FEM with Hermite-cubic elements for $N = 4, 8, 40, 80$.

5 Discussion

The temporal-convergence study (Section 4.1, Figure 1) confirms that our BDF2 integrator attains the expected second-order rate, with the error at $t = 1$ scaling as $O(\Delta t^2)$ (slope 1.99), whereas the Newmark- β implementation only achieves first-order behavior until $\Delta t \leq 0.025$. This result validates our choice of an A-stable BDF2 scheme for the stiff IBVP generated by the spatial discretization of the beam equation.

Spatial convergence (Section 3.2, Table 4, Figure 2) demonstrates fourth-order accuracy in h for Hermite-cubic elements, with the L^2 error decreasing from 4.52×10^{-6} at $N = 4$ to 9.01×10^{-11} at $N = 64$, and a fitted slope of approximately 4.0. The static-deflection comparison (Figure 3) further shows that even a coarse mesh ($N = 4$) captures the analytic profile qualitatively, and by $N = 40$ the FEM solution is visually indistinguishable from the exact deflection. Together, these studies confirm that moderate mesh resolutions ($N \geq 32$) suffice to achieve sub-percent errors in both deflection and internal loads, keeping computational cost manageable.

Our evaluation of simulation parameters in Section 4.2 ensured that all relevant physical and numerical scales are resolved. By enforcing $\Delta t \leq 0.01 H/U_\infty$, we keep temporal errors below 1%, and by choosing $h_e = L/32$ with $p = 3$ elements, spatial errors remain below 0.5%. ODE-solver tolerances $\text{rtol} = 10^{-6}$ and $\text{atol} = 10^{-8}$ balance accuracy in boundary-layer and structural solves against CPU cost. The fluid-structure coupling stability study showed that explicit partitioned iterations converge in fewer than 10 sub-iterations for $\Delta t \leq 0.05 H/U_\infty$ and nondimensional mass ratios $m^* \geq 0.3$, while under-relaxation factors $\omega \approx 0.8$ suppress added-mass instabilities at smaller m^* .

To determine the simulation parameters required for reliably resolving both aerodynamic and structural dynamics, we conducted a parametric sweep over time-step size Δt , mesh resolution $h_e = L/N$, and ODE

solver tolerances (rtol, atol). For the BDF2 integrator, we found that relaxing Δt beyond $0.01 H/U_\infty$ resulted in errors exceeding 1% in stall-onset time and peak lift, whereas $\Delta t \leq 0.005 H/U_\infty$ kept those errors below 0.5%. The Newmark- β scheme only recovered its nominal second-order convergence for $\Delta t \leq 0.0025 H/U_\infty$. On the spatial side, Hermite-cubic elements with $N \geq 32$ ($h_e \leq L/32$) produced L^2 deflection errors under 0.5%, with further mesh refinement yielding diminishing returns relative to cost. Finally, ODE tolerances of $\text{rtol} = 10^{-6}$ and $\text{atol} = 10^{-8}$ struck the best balance—doubling runtime relative to $\text{rtol} = 10^{-5}$ but improving peak-lift predictions by approximately 0.5%. Taken together, these studies motivate our recommended defaults of

$$\Delta t = 0.005 \frac{H}{U_\infty}, \quad N = 32, \quad p = 3, \quad \text{rtol} = 10^{-6}, \quad \text{atol} = 10^{-8},$$

which guarantee sub-percent accuracy while keeping computational effort practical.

These numerical results directly address the guiding questions from Section 2.1. For stall onset, reduced-order simulations (not shown) indicate that increasing pitch amplitude Θ leads to earlier onset times, while higher reduced frequency k delays the stall angle. This trend establishes a qualitative kinematic envelope in which more aggressive or faster pitching leads to earlier dynamic stall. For structural response to unsteady loads, our static deflection study (Figure 3) shows that the tip displacement scales consistently with applied load, suggesting that in the full FSI simulation, tip deflection amplitude is approximately proportional to the peak lift coefficient C_L . Sensitivity analysis revealed that perturbing the BL constant T_f significantly affects $C_{L,\max}$, while changes to τ_2 produce weaker responses. Similarly, temporal convergence plots (Figure 1) show that BDF2 maintains second-order accuracy even for relatively large time steps, whereas Newmark- β only achieves second-order convergence at finer Δt .

Coupling stability was evaluated by running staggered FSI iterations and counting sub-iterations to convergence. The results show stable behavior (within 5–10 sub-iterations) for mass ratios $m^* \geq 0.3$ and time steps $\Delta t \leq 0.05 H/U_\infty$, while cases with smaller m^* required Aitken under-relaxation with $\omega \in [0.7, 0.9]$. For load mitigation strategies, adding structural damping $\zeta = 0.1$ and using $\omega \approx 0.8$ reduced high-frequency lift transients, offering a practical route to smooth out dynamic spikes. The analysis of solver tolerances compared CPU cost to lift-prediction accuracy, showing that $\text{rtol} = 10^{-6}$ and $\text{atol} = 10^{-8}$ yield a good compromise—tight enough for high fidelity but not excessively expensive. For fatigue assessment, a 100-cycle simulation produced a bounded distribution of $C_{L,\max}$ values, with most cycles clustered near the mean and only rare excursions. These statistics inform fatigue-life modeling by quantifying the variability in load cycles. Finally, spatial resolution effects were characterized by the L^2 -error plot (Figure 2) and deflection comparisons (Figure 3), which confirm that Hermite-cubic elements with $N \geq 32$ provide sub-percent errors and visually exact agreement with the analytical solution.

Each investigation was grounded in quantitative error studies, convergence plots, and parameter sweeps. Together, they demonstrate that our numerical framework can faithfully simulate unsteady aeroelastic systems with robust accuracy, stability, and computational efficiency.

In summary, the combination of high-order spatial discretization, A-stable time integration, calibrated physical parameters, and targeted coupling strategies yields an FSI solver that is both accurate and efficient for dynamic-stall problems. Our results provide clear guidelines for mesh design, time-step selection, solver tolerances, and coupling protocols, enabling reliable prediction of unsteady aerodynamics and structural response under high-cycle loading.

6 Conclusion

In this project, we combined a dynamic-stall model with a beam model using high-order finite elements. Our tests showed that the BDF2 time integrator achieves second-order accuracy, while our current Newmark- β

scheme only reaches first-order accuracy and needs tuning. For the static beam under load, the Hermite–cubic elements delivered fourth-order spatial accuracy, with errors falling below 10^{-10} on fine meshes.

We also identified when our explicit fluid–structure coupling remains stable: without damping, it works up to a mass ratio of 0.4 and time steps of 0.02 s; by adding a simple under-relaxation and damping, stability extends up to a mass ratio of 0.7. Setting the ODE solver tolerance to 10^{-6} gave a good balance of speed and precision—under 0.6% error in peak lift and stall time at runtimes around 1.6 s per run. Running fifty cycles produced almost normal distributions for peak lift and displacement, providing useful data for fatigue-life estimates.

Overall, our approach is both accurate and efficient for studying dynamic stall. For better analysis results for next time, the next steps would include improving the Newmark– β accuracy, testing fully implicit coupling to reduce instabilities, and tuning model parameters with experimental data. We will also apply this framework to full rotor shapes, different flow conditions, and to UAV or wind-turbine designs.

Group Contributions

This project was a team effort; each member made contributions to at least one of the main tasks: problem formulation, numerical method derivation, code implementation, results analysis, and report preparation. The work split is as follows which is according to the rubric sections (1)–(6):

Sufyan Syed (20%): Led the formulation of the IBVP and derived the Hermite-cubic weak form in Section 2. Validated all physical assumptions and helped integrate the FEM and ODE code. He also created the repository on GitHub. His work significantly contributed to rubric sections (2), (3), and (6)

Samik Singh (20%): Implemented and tested the ODE solvers (BDF2 and Newmark– β) and carried out the temporal convergence study in Section 4. Generated Figure 1 and analyzed the convergence rates. Also worked on iterating the code for the numerical method, and the results. His work significantly contributed to rubric sections (1), (2) and (3)

Benjamin Litvak (20%): Managed the overall LaTeX formatting and wrote all mathematical notation. Organized figures, tables, and ensured reproducibility of code snippets throughout the report. Also worked on iteration with the numerical method as well as work on the group contributions in section (5). His work significantly contributed to rubric sections (2), (4), and (5)

Angelina Yan (20%): Developed the FEM code for static beam deflection and conducted the spatial-convergence study. Produced Figure 3, Table 4, and associated discussion in Section 4. Also helped work on iterating the code for our initial presentation of our IBVP as well as the algorithmic summary for our numerical method. Her work significantly contributed to rubric sections (1), (2), and (3)

Suraj Duvvapu (20%): Helped draft the overall report, interpreting error trends and making mesh/time-step recommendations. Coordinated the final peer review, ensuring consistency and technical accuracy. Also aided in the iteration of the numerical method in section 2 as well as explaining our mathematical model and simulation set up. His work greatly contributed to rubric sections (3), (4), and (5).

All members reviewed the final draft, provided feedback on every section, and approved the document before submission. Contribution percentages reflect the time spent on research, coding, writing, and coordination.

Appendix

The complete Python code for the simulations and figure generation is included in the supplementary file(AE370 Project Code Report.ipynb). The project code and detailed documentation are available on our GitHub repository: https://github.com/ssyed68/AE370_Project2.

References

[1] Melani, P. F., Aryan, N., Greco, L., and Bianchini, A., “The Beddoes-Leishman Dynamic Stall Model: Critical Aspects in implementation and calibration,” *Renewable and Sustainable Energy Reviews*, vol. 202, Sep. 2024, p. 114677.

The python code that was used for this project was done with the help of ChatGPT. We specifically used ChatGPT to help us with using BDF2 and FEM, as well as helping us with our methods and our plots for the results portion.